

# Multiscale observation in wide-spatial radar surveillance based on coherent FDA design

Lei YU, Feng HE\* &amp; Yi SU

*College of Electronics Science, National University of Defense Technology, Changsha 410035, China*

Received 18 August 2022/Revised 8 February 2023/Accepted 27 June 2023/Published online 25 January 2024

**Abstract** Wide-spatial radar surveillance missions are challenging tasks, requiring an increased power budget and agility in transmission aimed at extracting information from multiple targets in different environments. These requirements necessitate high transmitting degrees of freedom (DOF) to achieve the objective of multiscale observation for specific tasks in specialized regions of interest. Herein, we exploit the multiscale observation ability in wide-spatial radar surveillance based on frequency diverse array (FDA) radar. The proposed method facilitates spatial anisotropic control of multiple radar resources, including the transmitting waveforms, beam pattern, and bandwidth. By utilizing a coherent FDA radar, we offer principles for the selection of baseband waveforms, in addition to the quantitative design of the beam pattern gain and optimal bandwidth from the perspective of detection. The feasibility of the proposed method is validated through numerical experiments, thus indicating the potential in wide-spatial radar surveillance. Moreover, this work can be regarded as a preliminary attempt to gauge the efficacy of the computational array, a novel academic concept.

**Keywords** multi-scale observation, wide-spatial surveillance, frequency diverse array (FDA), beam pattern synthesis, frequency diversity gain, computational array

## 1 Introduction

Wide-spatial surveillance radar involves the extraction of target information (for detection or identification) in long-range and large observation fields [1, 2]. The primary benefits of wide-spatial coverage include excellent detectability of multiple interested targets, angular diversity gain, and enhanced Doppler resolution, which is especially valuable in being able to distinguish slow-moving targets from clutter and noise [3]. However, there are several difficulties associated with wide-spatial observation; these issues arise due to the substantial variability of the characteristics of target, clutter, and interference in complex environments. To overcome these challenges, the advanced surveillance radar system must be able to not only optimize the power budget but also improve the multiscale observation ability, which implies the flexible and anisotropic control of multiple transmitting resources, including waveform, beam pattern, and bandwidth [4–6]. The main advantages of multiscale observation can be demonstrated through the following example. Considering a ground-based surveillance radar steering beam in elevation, the waveform designed for low-altitude regions must encounter strong surface clutter. Meanwhile, for high-altitude regions, the transmitting waveform must possess sufficient Doppler tolerance to maintain the detection performance of high-speed aerial targets (such as low-orbit satellites and hypersonic missiles). Furthermore, from the perspective of wideband observation, a high range resolution is beneficial not only in target identification and clutter suppression but also in frequency diversity gain [7–12]. Several studies have demonstrated that the optimal detection bandwidth depends on the number of independent samples and fluctuation characteristics of targets (from Swerling 0 to Swerling 4) [8–10]. With regard to the aforementioned factors, multiscale observation may help achieve superior performance in wide-spatial surveillance. A similar perspective is proposed in a novel research field, referred to as the computational array [4], which also sheds light on the performance enhancement arising due to high transmitting degrees of freedom (DOF).

---

\* Corresponding author (email: [hefeng@nudt.edu.cn](mailto:hefeng@nudt.edu.cn))

To realize wide-spatial coverage, the technique of broadened beam illumination in a transmitter is utilized in a standard digital beamforming (DBF) radar, such as a ubiquitous and holographic radar [13–15]. For such radar, the transmitting directivity is traded against broad angular coverage, which means longer integration time, higher Doppler resolution, and better visibility of the fluctuation target. However, omnidirectional transmission possesses several limitations. First, the broadened beam results in mainlobe clutter and jamming. Because the directivity in the transmitting side cannot be utilized, the widened mainlobe weakens the rejection of clutter and jamming by half (only the receive beamforming can be used to suppress the sidelobe clutter) [3]. Furthermore, widened beam illuminates identical waveforms in all directions isotropically. As discussed previously, this is not an optimal approach for wide-spatial observation. Finally, in this situation, once the transmit beampattern is designed, the transmit power in spatial will be immobilized, which implies that the detectable range is fixed and cannot be adjusted for emergent situations dynamically.

Another widely researched solution for instantaneous wide-spatial coverage is the orthogonal multiple-input multiple-output (MIMO) radar, which synthesizes the omnidirectional beampattern by transmitting orthogonal waveforms in all independent channels [16]. In a more generalized context, the orthogonal constraint can be relaxed, and the covariance matrix of correlated MIMO waveforms can be optimized to synthesize the transmit beampattern according to the desired shape [17–19]. The MIMO radar also possesses several limitations in wide-spatial surveillance. First, it is difficult to realize a strictly orthogonal waveform in practice, which leads to non-uniform distribution of transmitting gain, and the constant modulus constraint may not be rigorously adhered to in MIMO radar waveform design [20]. Besides, the computational complexity in the optimization process exponentially increases according to the scale of transmit elements, further restricting its practicability [21]. Finally, neither the orthogonal nor correlated MIMO radar can specify the transmitting waveforms and bandwidths anisotropically in specialized directions. Consequently, achieving the ideal multiscale observation in wide-spatial surveillance remains a challenging task for conventional MIMO radar systems.

Recent studies on waveform diversity array and space-time coding technologies have attempted to address the aforementioned issues in wide-spatial surveillance [22–35]. Among these studies, the frequency diverse array (FDA) radar has garnered considerable attention due to its beam agility, computational convenience, and additional DOF in transmission. By introducing a specialized incremental frequency bias between the transmit elements, coherent FDA (here, it means that the transmitted baseband waveforms in different channels are strictly coherent) radar performs intrapulse beam scanning in spatial. Furthermore, based on a combination with MIMO waveform design, the FDA-MIMO radar may be beneficial in range-angle joint localization [26, 27], range ambiguous clutter suppression [28, 29], and mainlobe interference suppression [30–32]. The recent research roughly indicates that the beam agility of coherent FDA radar can be further exploited [33]. Consequently, coherent FDA radar, capable of increasing target extraction and identification performance in wide-spatial surveillance systems, serves as an adequate choice for multiscale observation.

Herein, we focus on the quantitative design of coherent FDA radar developed for multiscale observation and wide-spatial surveillance by exploiting transmit DOFs. The proposed method not only provides the solution for spatial waveform diversity but also presents the waveform selection principles in coherent FDA. Furthermore, the quantitative design of beampattern gain in specialized regions of interest (ROI) is proposed to achieve the detectable range extension. Finally, based on the prior knowledge of the interested targets, the theoretical analysis of frequency diversity gain is introduced with the aim of optimizing the spatial bandwidth allocation of coherent FDA radar. In our previous work [36], a qualitative prospect is presented. The primary contributions of this paper are listed below:

- A multiscale observation method is proposed and introduced into wide-spatial radar surveillance based on coherent FDA radar. Principles of waveform selection in coherent FDA radar are provided.
- Based on coherent FDA radar, the quantitative design of beampattern gain in specialized ROI is first developed and further applied in detectable range extension.
- Based on coherent FDA radar, the quantitative analysis of optimal observation range resolution and frequency diversity gain is introduced to optimize the spatial bandwidth allocation and subsequently achieve improved detection performance.
- This work presents a reasonable prototype in the field of computational arrays [4]. In this novel concept, the idea of high transmitting DOFs and the architecture of “element-module-system” can be embodied in this work.

The remainder of this paper is organized as follows. In Section 2, the basic properties of coherent

FDA radar to realize the spatial waveform diversity are introduced, and the principles of waveform selection in coherent FDA are proposed. In Section 3, the quantitative beampattern design and spatial detectable range extension method are presented. In Section 4, the practical range resolution in coherent FDA and the frequency diversity gain are analyzed for spatial bandwidth allocation in a quantitative manner. Numerical simulations are presented in Section 5. Section 6 provides a detailed explanation of the relationship between this work and the computational array. Finally, in Section 7, the main conclusion has been presented.

## 2 Signal model of coherent FDA radar and spatial transmit waveform diversity

In this section, the signal model of coherent FDA is presented to illustrate its basic characteristics. Then, the realization of spatial waveform diversity and the principles of waveform selection in coherent FDA radar are proposed.

### 2.1 Signal model of coherent FDA radar

Considering an uniform linear array (ULA) with  $M$  elements and half-wavelength interspace  $d$ , for coherent FDA radar, the carrier frequency in the  $m$ th transmitting channel is

$$f_m = f_0 + (m - 1) \Delta f, \quad m = 1, 2, \dots, M, \quad (1)$$

where  $f_0$  is the reference central frequency and  $\Delta f$  is the incremental frequency bias which is assumed identical in adjacent elements. The transmitted signal in the  $m$ th channel yields

$$s_m(t) = \text{rect} \left( \frac{t}{T_p} \right) \varphi(t) \exp(j2\pi f_m t), \quad (2)$$

where  $\text{rect}(x) = \begin{cases} 1, & |x| \leq 0.5 \\ 0, & |x| > 0.5 \end{cases}$  is the window function and  $T_p$  is the pulse duration.  $\varphi(t)$  is the baseband waveform, which is identical in different channels. With the signal propagation, the integrated signal at  $(r, \theta)$  in far-field can be expressed as follows:

$$\begin{aligned} x(\theta, t - \tau) &= \xi_t \cdot \sum_{m=1}^M s_m(t - \tau_m) \\ &\approx \xi_t \cdot \text{rect} \left( \frac{t - \tau}{T_p} \right) \varphi(t - \tau) \cdot \sum_{m=1}^M \exp \left\{ j2\pi f_m \left( t - \tau + \frac{(m - 1) d \sin \theta}{c} \right) \right\}, \end{aligned} \quad (3)$$

where  $\xi_t$  is the propagation coefficient,  $\tau = r/c$  is the consistent range delay. Based on narrowband assumption, we have  $\tau_m = \tau - (m - 1) d \sin \theta / c$ .

Based on that an approximation is introduced into the accumulation term in (3) and yields

$$x(\theta, t - \tau) \approx \xi_t \cdot \text{rect} \left( \frac{t - \tau}{T_p} \right) \varphi(t - \tau) \exp(j2\pi f_0 (t - \tau)) \cdot P_t(\theta, t - \tau), \quad (4)$$

where

$$P_t(\theta, t - \tau) = \exp \left\{ j(M - 1) \pi \left( \Delta f (t - \tau) + \frac{d \sin \theta}{\lambda_0} \right) \right\} \cdot \frac{\sin \left( M \pi \left( \Delta f (t - \tau) + \frac{d \sin \theta}{\lambda_0} \right) \right)}{\sin \left( \pi \left( \Delta f (t - \tau) + \frac{d \sin \theta}{\lambda_0} \right) \right)}, \quad (5)$$

where  $\lambda_0$  is the wavelength corresponding to the reference frequency  $f_0$ .

As is illustrated in (4),  $P_t(\theta, t - \tau)$  appears as a complex-valued beampattern correlated with fast time, range delay, and angular direction. Compared with phased array (PA) radar, the transmitted signal of coherent FDA radar is not only spatially modulated by  $|P_t(\theta, t)|$ , but also temporally modulated by the complex-valued phase term in (5). A demonstration of space-time coupled beampattern of FDA and time-frequency diagrams of transmitted signal (assuming the baseband waveform is linear frequency modulated (LFM)) in three different directions are illustrated in Figure 1.

It is clearly demonstrated in Figure 1 that the mainlobe orientation of the FDA beampattern varies from  $-\pi/2$  to  $\pi/2$  within the pulse duration, which covers the entire observation field and maintains

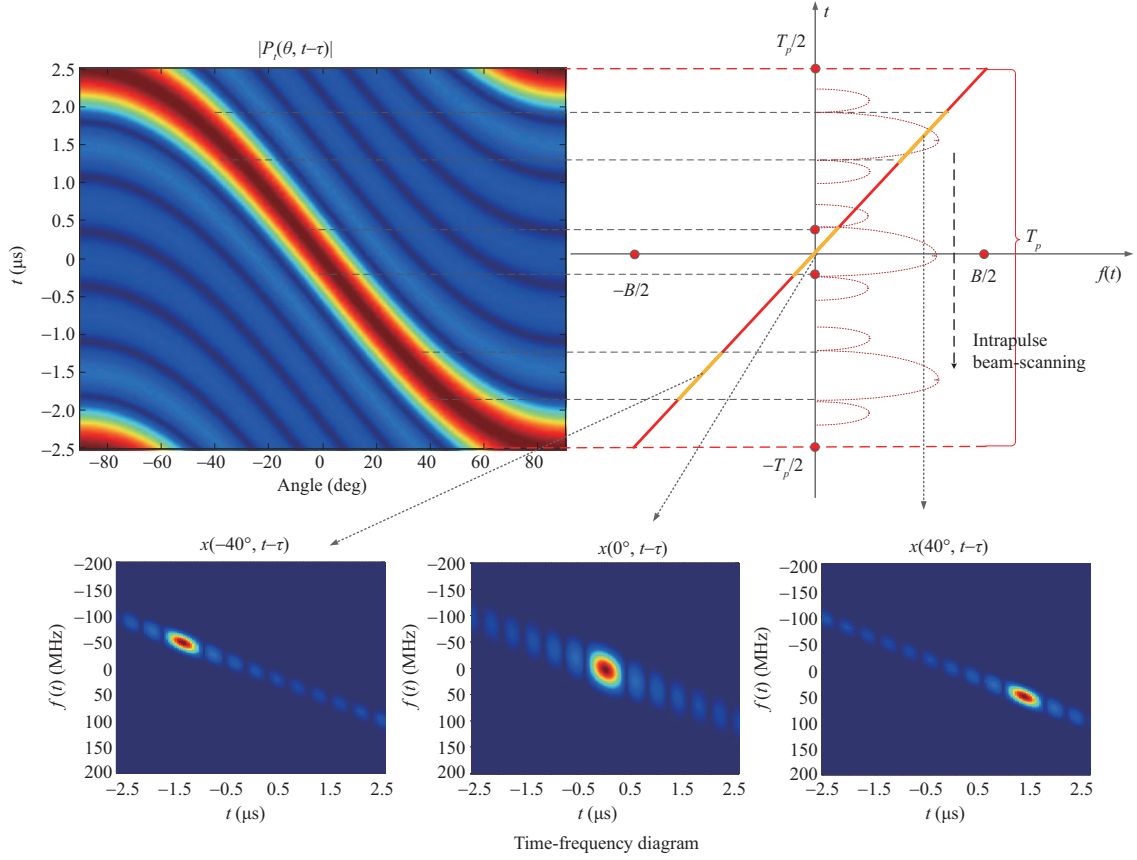


**Figure 1** Space-time coupled FDA transmit beampattern and the time-frequency diagrams of the transmitted signal in  $-40^\circ$ ,  $0^\circ$ , and  $40^\circ$ .

transmit directivity at the same time. By further derivation upon (5), the relationship between beam orientation  $\theta$ , fast time  $t$  and range delay  $\tau$  can be expressed as

$$\theta = \arcsin \left[ \frac{\lambda_0}{d} (k + \Delta f (t - \tau)) \right], \quad k \in \mathbb{Z}, \quad (6)$$

where  $k$  is an integral variable and  $\mathbb{Z}$  denotes the set of integer.

It can be seen from (6) that the mainlobe of FDA radar uniformly scans in angular domain with a sinusoidal angular velocity  $\omega_\theta = \partial \sin \theta / \partial t = \lambda_0 \Delta f / d$ . Let  $\Omega = [\sin \theta_{\min}, \sin \theta_{\max}]$  represent beam-scanning interval and  $\Theta = |\sin \theta_{\max} - \sin \theta_{\min}|$  denote the length of interval, where  $\theta_{\min}$  and  $\theta_{\max}$  represent the starting and ending point of the interval.  $\Theta$  is determined by the frequency offset  $\Delta f$  with the following relationship:

$$\Theta = T_p \lambda_0 \Delta f / d. \quad (7)$$

In essential, the spatial and temporal modulation of FDA beampattern acts as a windowing function on transmitted baseband waveform. As is shown in Figure 1, due to the fast intrapulse beam-scanning, transmitted baseband waveform in different instantaneous is spatially weighted and illuminated in different directions. To illustrate the windowing effect, the time-frequency diagrams of transmitted signals in three different directions ( $-40^\circ$ ,  $0^\circ$ , and  $40^\circ$ ) are presented in Figure 1. It is demonstrated that in each direction the practical synthetic signal is actually a piece of the entire LFM waveform, which is led by the windowing effect in space-time dimensions.

## 2.2 Realization of spatial waveform diversity and principles of waveform selection in coherent FDA

Space-time coupled characteristic of FDA radar motivates us to realize the spatial waveform diversity by designing an integrated signal consists of multiple subpulses which correspond to different angular sectors.

In each subpulse, the baseband waveform can be independently designed according to the properties of targets and environments. The detailed designing process is presented in the following.

Firstly, the entire observation filed is divided into  $L$  angular sectors, where  $\Omega = \sum_{l=1}^L \Omega_l$ ,  $\Theta = \sum_{l=1}^L \Theta_l$  and  $\Theta_l = |\sin \theta_{\max,l} - \sin \theta_{\min,l}|$ . Considering consistent frequency offset in subpulses, the  $l$ th subpulse duration  $T_{p,l} = \frac{\Theta_l}{2\Delta f}$  is determined by the range of angular sector  $\Theta_l$  and the frequency offset  $\Delta f$  jointly. Following that, the set of subpulse waveforms  $\{\varphi_1(t), \varphi_2(t), \dots, \varphi_L(t)\}$  are designed for each angular sector independently. Finally, integrating all subpulses and the transmitted signal designed for the  $m$ th element is given as follows:

$$s_m(t) = \sum_{l=1}^L \text{rect}\left(\frac{t - \eta_l}{T_{p,l}}\right) \varphi_l(t - \eta_l) \exp(-j2\pi f_m t), \quad (8)$$

where  $\eta_l$  is the  $l$ th time-shift to separate each subpulse, yields

$$\eta_l = (-T_p + T_{p,l})/2 + \sum_{i=1}^{l-1} T_{p,i}. \quad (9)$$

Based on the implementations above, the designed multiple waveforms  $\{\varphi_1(t), \varphi_2(t), \dots, \varphi_L(t)\}$  are sequentially transmitted into different angular sectors within the pulse duration and the spatial waveform diversity is accomplished.

Another important question that has been rarely discussed is the principles of waveform selection in coherent FDA radar. Since the intrapulse beam-scanning has different effects on frequency modulated (FM) and phase-coded waveforms, it is worthwhile to present qualitative principles to instruct the waveform selection in coherent FDA.

Considering the transmitted signal model in (8), a space-time matched function is designed as follows [24]:

$$f(\theta_0, t) = \mathbf{a}_t^H(\theta_0) \mathbf{S}^*(-t), \quad (10)$$

where  $\mathbf{a}_t(\theta_0) = [1, e^{-j2\pi \frac{d \sin \theta_0}{\lambda_0}}, \dots, e^{-j2\pi(M-1) \frac{d \sin \theta_0}{\lambda_0}}]^T$  is the steering vector of transmit array and  $\mathbf{S}(t) = [s_1(t), s_2(t), \dots, s_M(t)]^T$  is the transmitted signal vector.

Furthermore,  $\xi_t = 1$  and  $\theta = \theta_0$  are assumed and the matched filtered signal of  $x(\theta, t - \tau)$  by  $f(\theta_0, t)$  yields

$$\begin{aligned} y'(\theta, \theta_0, t - \tau)|_{\theta=\theta_0} &= x(\theta, t - \tau) \otimes f(\theta_0, t) \\ &= \underbrace{\sum_{m=1}^M \int_{-T_p/2}^{T_p/2} \psi(t) \psi^*(t - \tau) dt}_{\text{self-term}} + \underbrace{\sum_{m=1}^M \sum_{n \neq m}^M \int_{-T_p/2}^{T_p/2} \psi(t) \psi^*(t - \tau) \cdot e^{-j2\pi(m-n)\Delta f t} dt}_{\text{cross-term}}, \end{aligned} \quad (11)$$

where  $\otimes$  denotes the convolution and  $\psi(t) = \sum_{l=1}^L \varphi_l(t)$  is the integrated baseband waveform.

As is shown in (11), the self-term corresponds to the autocorrelation of baseband waveform, and the cross-term can be considered as the ambiguity function (AF) of  $\psi(t)$  with an equivalent Doppler frequency  $f_d = (m - n) \Delta f$ . As for the FM waveform with oblique ridge-shaped AF, a slight Doppler-shift in matched filtering will lead to the range-shift in the impulse response. Consequently, the mainlobe of cross-terms will be shifted along the range and merged into the adjacent sidelobe of self-terms. This results in the mainlobe expansion, which leads to the degradation of range resolution. In return, the peak-to-sidelobe ratio (PSLR) will be significantly improved. On the contrary, phase-coded signal with thumbtack-shaped AF will suffer the PSLR aggravation when it is used in coherent FDA. This is due to the fact that equivalent Doppler-shift in cross-terms will lead to the dramatic decrease of mainlobe response and the arise of noise pedestal. Fortunately, as for phase-coded signal in coherent FDA, the observation range resolution will not be influenced, since the range resolution of phase-coded waveform is only determined by code width. Furthermore, PSLR aggravation in this case can be mitigated by mismatched filter design in the receiver.

In summary, the phase-coded waveform with thumbtack-shaped AF will maintain the range resolution at the price of PSLR aggravation, and the FM waveform with oblique ridge-shaped AF will acquire significant PSLR improvement but suffer the mainlobe expansion in range. In both cases, the declination

of time-bandwidth production (TBP) will be introduced. These waveform selection principles of coherent FDA are quantitatively validated by numerical simulations in Section 5.

### 2.3 Received signal processing of coherent FDA radar

A collocated half-wavelength ULA with  $N$  elements is considered in the receiver. After down conversion with reference frequency  $f_0$ , the received signal in the  $n$ th element from a target locating at  $(r, \theta)$  can be expressed as

$$y_n(\theta, t - \tau_r) = \xi_r \cdot \text{rect}\left(\frac{t - \tau_r}{T_p}\right) \varphi(t - \tau_r) \exp(-j2\pi f_0 \tau_r) \cdot \exp\left\{-j2\pi(n-1) \frac{d \sin \theta}{\lambda_0}\right\} \cdot P_t(\theta, t - \tau_r), \quad (12)$$

where  $\tau_r = 2r/c$  is the round-trip range delay and  $\xi_r$  is the round-trip propagation coefficient.

Combining the received signal in all elements, the  $N$ -dimensional signal vector is derived as

$$\mathbf{Y}(\theta, t - \tau_r) = \xi_r \cdot \mathbf{a}_r(\theta) \text{rect}\left(\frac{t - \tau_r}{T_p}\right) \varphi(t - \tau_r) \cdot \exp(-j2\pi f_0 \tau_r) \cdot P_t(\theta, t - \tau_r), \quad (13)$$

where  $\mathbf{a}_r(\theta) = [1, e^{-j2\pi \frac{d \sin \theta}{\lambda_0}}, \dots, e^{-j2\pi(N-1) \frac{d \sin \theta}{\lambda_0}}]^T$  is the steering vector of receive array.

Normally, the receive DBF, similar to the ubiquitous radar, can be operated at first for angular discrimination as follows:

$$r(\theta, \theta_0, t - \tau_r) = \xi_r \cdot \mathbf{w}_r^H(\theta_0) \mathbf{a}_r(\theta) \text{rect}\left(\frac{t - \tau_r}{T_p}\right) \cdot \varphi(t - \tau_r) \exp(-j2\pi f_0 \tau_r) \cdot P_t(\theta, t - \tau_r), \quad (14)$$

where  $\mathbf{w}_r(\theta_0) = [1, e^{-j2\pi \frac{d \sin \theta_0}{\lambda_0}}, \dots, e^{-j2\pi(N-1) \frac{d \sin \theta_0}{\lambda_0}}]^T$  is the beamforming vector at  $\theta_0$ .

Different from ubiquitous radar, the wide spatial coverage of coherent FDA is achieved by intrapulse beam-scanning with a pencil-shaped beam. Consequently, the transmitting directivity is preserved and can be recovered by the following space-time matched-filter [24]:

$$h(\theta_0, t) = \sum_{m=1}^M e^{-j2\pi(m-1) \left(\Delta f t + \frac{d \sin \theta_0}{\lambda_0}\right)} \cdot \varphi(t). \quad (15)$$

Actually,  $h(\theta_0, t)$  incorporates the equivalent transmit DBF in spatial and pulse compression in range simultaneously. The received signal after space-time matched filtering yields

$$r_{\text{pc}}(\theta, \theta_0, t - \tau_r) = r(\theta, \theta_0, t - \tau_r) \otimes h^*(\theta_0, -t). \quad (16)$$

Note that through receive DBF and space-time matched filtering, the angular discrimination ability of coherent FDA is equivalent with orthogonal MIMO radar. The complete receive signal processing procedures of coherent FDA are demonstrated in Figure 2, where  $N_\theta$  denotes the number of output signal in receive DBF.

## 3 Quantitative design for beampattern synthesis and detectable range extension based on coherent FDA

In this section, a quantitative beampattern synthesis method for coherent FDA radar is proposed, which enables the designer to alternate beampattern gain in each ROI independently. On this basis, the detectable range extension method in specialized ROI is proposed. That will help the surveillance radar acquire better visibility in emergent situation dynamically. Compared with the qualitative method in [33], the quantitative design of beampattern gain in independent ROI is proposed for the first time.

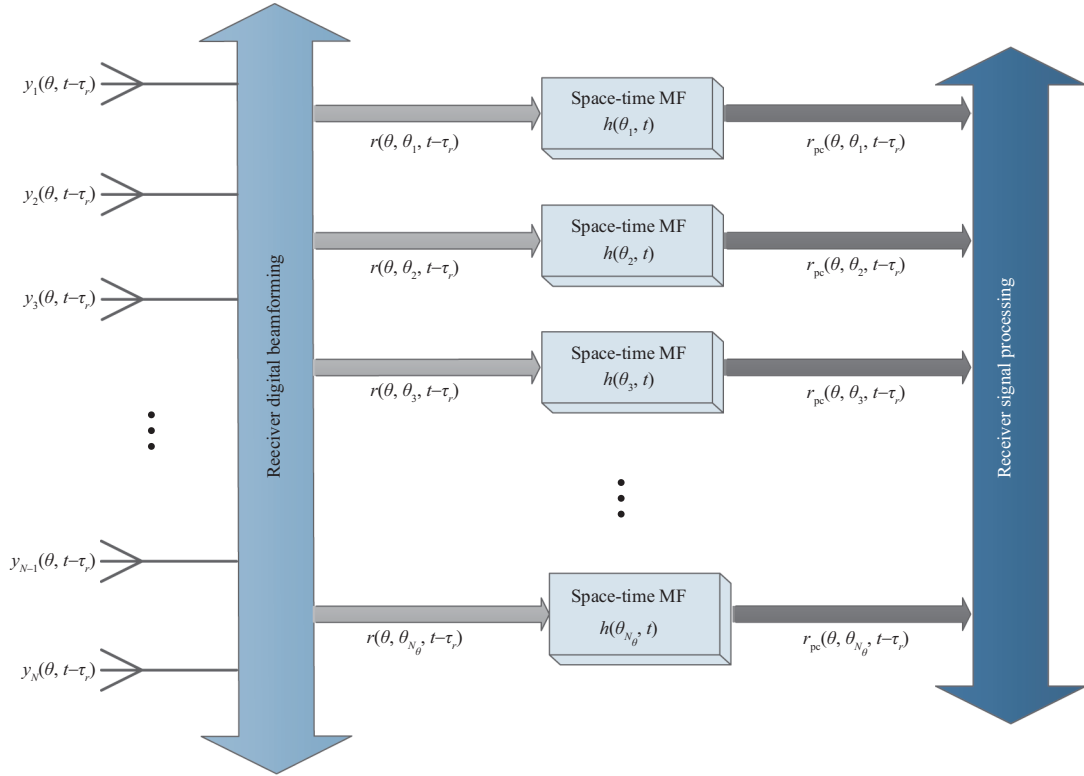


**Figure 2** Receive signal processing procedures of coherent FDA radar.

### 3.1 Principles of transmit beampattern synthesis based on coherent FDA

Beampattern synthesis in correlated MIMO radar usually requires complicated processes [17–19], including the signal covariance matrix optimization, and multi-channel waveforms generation. This kind of method has at least two limitations. Firstly, the high-dimensional optimization will increase the computational burden, especially for large-scale system. Secondly, the spatial waveform diversity cannot be further exploited. Essentially, the transmit beampattern synthesis can be resolved in a straightforward approach. As a matter of fact, the spatial allocation of transmitting energy is determined by the product of transmit power and the mainlobe illumination time (that also explains why the PA radar has the highest directional gain).

Increased beam agility of coherent FDA radar provides the opportunity to synthesize transmit beampattern directly. According to (6), the angular velocity of intrapulse beam-scanning is determined by the frequency offset  $\Delta f$ . That means by alternating  $\Delta f$  within the pulse duration, the mainlobe illumination time in specialized ROI can be prolonged to acquire higher beampattern gain in this ROI. Compared with MIMO beampattern synthesis, the computational complexity is alleviated and additional DOF in the waveform domain is released. To realize the quantitative design of beampattern gain in ROI, the adjustable beam-scanning velocity is required within the pulse duration. That means the frequency offsets and the subpulse durations need to be redesigned specifically. The detailed implementations are presented as follows.

Firstly, considering the set of spatial incontinuous ROI,  $\Omega_{\text{ROI}} = \{\Omega_1, \Omega_2, \dots, \Omega_K\}$ , and  $K$  is the number of ROI. Thus, the entire observation field is segmented into  $L' = 2K + 1$  independent angular sectors. We define  $\tilde{\Omega}_{\text{ROI}}$  to represent the set of uninterested regions, which includes  $K + 1$  angular sectors outside of the ROI. The union set of  $\Omega_{\text{ROI}}$  and  $\tilde{\Omega}_{\text{ROI}}$  is the entire observation field, i.e.,  $\Omega = \Omega_{\text{ROI}} \cup \tilde{\Omega}_{\text{ROI}}$ . Then, the subpulse durations are defined as  $[T_{p,1}, T_{p,2}, \dots, T_{p,L'}]$ , s.t.  $T_p = \sum_{l=1}^{L'} T_{p,l}$ , where  $T_{p,l}$  corresponds to the mainlobe illumination time in the  $l$ th angular sector. Following that the frequency offset in each subpulse is redesigned as  $\Delta f_l = \Theta_l / 2T_{p,l}$ . Finally, the integrated transmitted signal for the  $m$ th element is expressed as

$$s_m(t) = \sum_{l=1}^{L'} \text{rect}\left(\frac{t - \eta_l}{T_{p,l}}\right) \varphi_l(t - \eta_l) \exp(-j2\pi f_{m,l}t), \quad (17)$$

where

$$\begin{cases} f_{m,l} = f_0 + (m-1)\Delta f_l = f_0 + (m-1)\frac{\Theta_l}{2T_{p,l}}, \\ \eta_l = (-T_p + T_{p,l})/2 + \sum_{i=1}^{l-1} T_{p,i}. \end{cases} \quad (18)$$

For convenience, only the subpulse durations corresponding to the ROI are required to be assigned specifically and the frequency offset designed for the uninterested angular regions yields

$$\Delta f_{\tilde{\Omega}_{\text{ROI}}} = \frac{\tilde{\Theta}_{\text{ROI}}}{2(T_p - \sum_{k=1}^K T_{p,k})}, \quad (19)$$

where  $\tilde{\Theta}_{\text{ROI}} = \sum_{j=1}^{K+1} \Theta_j$  and  $\Theta_j$  corresponds to the uninterested angular region  $\Omega_j \subset \tilde{\Omega}_{\text{ROI}}$ .

Furthermore, for quantitative analysis of beampattern gain, the one-dimensional equivalent beampattern of FDA is proposed and defined as the intrapulse integration in the time-domain as follows:

$$g(\theta) = \frac{1}{T_p} \int_{-T_p/2}^{T_p/2} |P_t(\theta, t)|^2 dt, \quad (20)$$

where  $g(\theta)$  can be explained as the temporal average of  $P_t(\theta, t)$  and it has the same physical definition with the array beampattern in traditional meaning. For example, the beampattern of the PA radar calculated by (20) is equal to the result derived by the steering vector.

Considering the intrapulse beam-scanning property of FDA, the one-dimensional equivalent beampattern  $g(\theta)$  is able to evaluate the average directional gain in transmission. Analytical expression of  $g(\theta)$  is derived by calculating the antiderivative of integral in (20) as follows:

$$\begin{aligned} \Xi(\theta, t) &= \frac{1}{T_p} \int |P_t(\theta, t)|^2 dt \\ &= \frac{1}{2\pi\Delta f M T_p} \left| e^{j2M\pi(\Delta f t + \frac{d \sin \theta}{\lambda_0})} \cdot {}_2F_1\left(1, M, 1+M, e^{j2\pi(\Delta f t + \frac{d \sin \theta}{\lambda_0})}\right) \right. \\ &\quad \left. + M \ln\left(1 - e^{-j2\pi(\Delta f t + \frac{d \sin \theta}{\lambda_0})}\right) \right|^2, \end{aligned} \quad (21)$$

where  ${}_2F_1(a, b, c, z)$  is the hypergeometric function [37].

An qualitative demonstration is presented in Figure 3 by assuming  $K = 1$  and ROI is  $[0^\circ, 20^\circ]$ . According to the analysis above, the mainlobe illumination time in ROI is set as  $T_{p,k} = 0.3T_p, 0.5T_p$ , and  $0.7T_p$ , respectively. Comparisons of transmit beampatterns are demonstrated in Figure 3. It is clearly illustrated that by prolonging the illumination time in specialized ROI, beampattern gains in these directions are significantly increased. For example, in the case of  $T_{p,k} = 0.7T_p$ , the beampattern gain in  $[0^\circ, 20^\circ]$  is 8.98 dB higher than the referenced value (corresponds to the uniform beam-scanning when  $\Delta f = 1/T_p$ ).

### 3.2 Quantitative design of beampattern gain and detectable range extension in ROI

In the previous discussion, it was revealed that the beampattern gain in specialized ROI can be improved by introducing the adjustable beam-scanning velocity in subpulses. However, it is only a qualitative demonstration. In the following, the quantitative design of FDA beampattern gain in ROI is developed and further applied in detectable range extension.

First of all, the idealized beampattern gain  $G_{\text{id}}(\Omega_{\text{ROI}})$  for ROI are preassigned. Strictly speaking,  $G_{\text{id}}(\Omega_{\text{ROI}})$  can be designed in any desired shape with reasonable gain. Normally, it is more practical to shape  $G_{\text{id}}(\Omega_{\text{ROI}})$  into rectangular functions with consistent gain in specific ROI. Then, based on (20), the iterative operation can be implemented to resolve the following optimization problem:

$$\begin{aligned} &\arg \min_{[T_{p,1}, T_{p,2}, \dots, T_{p,K}]} \|G_{\text{id}}(\Omega_{\text{ROI}}) - g(\Omega_{\text{ROI}})\|_2 + \gamma \|G_l - g(\tilde{\Omega}_{\text{ROI}})\|_2 \\ &\text{s.t. } G_l < g(\Omega_{\text{ROI}}) < G_u, \end{aligned} \quad (22)$$

where  $g(\Omega_{\text{ROI}})$  and  $g(\tilde{\Omega}_{\text{ROI}})$  represent the synthesized beampattern within and without the ROI.  $G_u$  is the upper bound of beampattern gain which is calculated in PA mode and  $G_l$  is the lower bound value

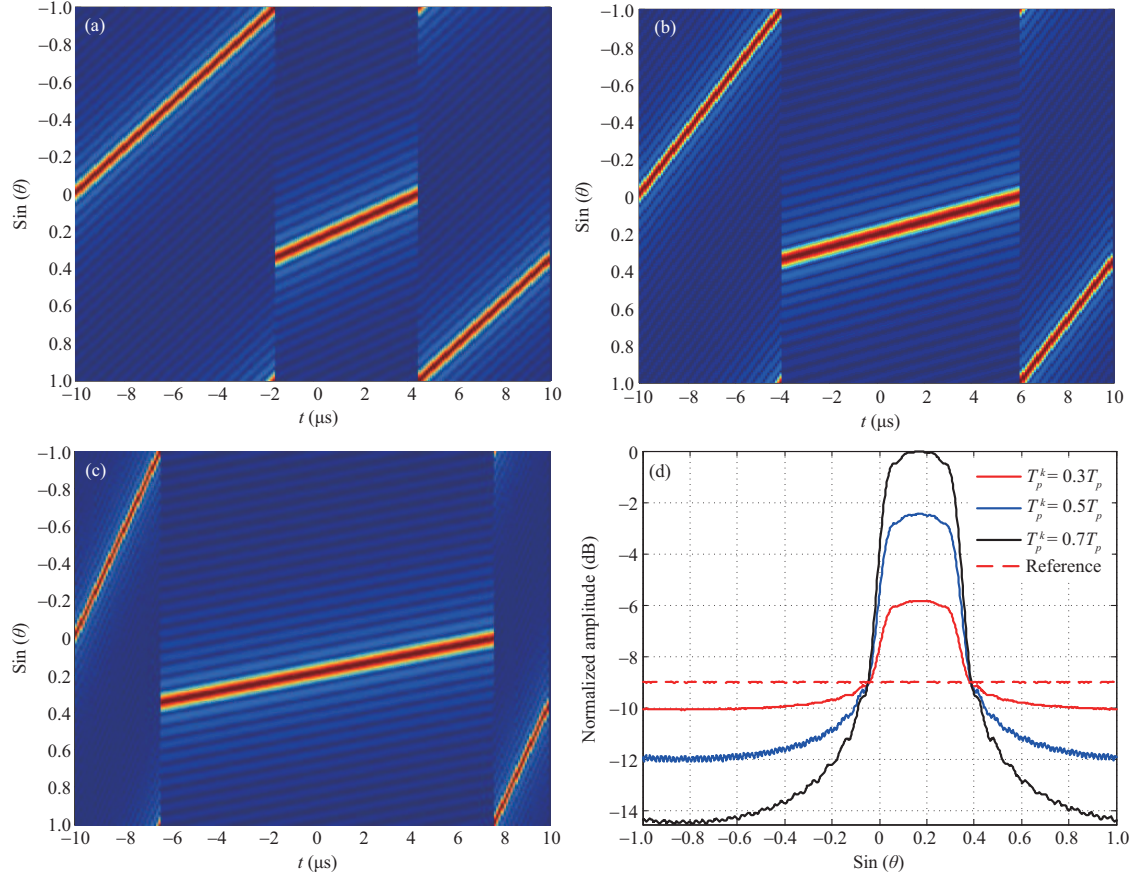


**Figure 3** Space-time transmit beampatterns of coherent FDA radar with different subpulse durations allocation. (a)  $T_{p,k} = 0.3T_p$ ; (b)  $T_{p,k} = 0.5T_p$ ; (c)  $T_{p,k} = 0.7T_p$ ; (d) comparison of the one-dimensional equivalent FDA beampatterns.

derived when  $\Delta f = 1/T_p$ .  $\gamma$  is the regularization parameter. Eq. (22) can be solved by basic sequential operations. Furthermore, it is revealed that the variables to be optimized are the subpulse durations correspond to ROI, due to the fact that  $T_{p,k}$  determines the illumination time in the  $k$ th angular sector.

Based on the quantitative synthesis of beampattern gain, the detectable range extension in ROI can be developed according to the Shnidman empirical function [38]. Shnidman function calculates the minimum single-pulse SNR (signal noise ratio) required for expected detection performance, including the probability of detection  $P_d$ , false alarm probability  $P_{fa}$ , integration number  $n_p$ , and the Swerling type of target. The detailed structure of the Shnidman function is discussed in Appendix A and it is used to calculate the minimum required single-pulse SNR in this problem. Finally, the surveillance radar range equation in (23) is applied to calculate the required beampattern gain  $G_{id}(\Omega_{ROI})$  for detectable range  $R_{id}$ .

$$R_{id}^4 = \frac{G_{id}(\Omega_{ROI}) \cdot P_{av} G_r \lambda_0^2 \delta I(n_p)}{(4\pi)^3 k T_0 F_n L_t L_f \cdot (SNR)_l} \cdot T_r, \quad (23)$$

where  $T_r$  is the pulse repetition time.

As one of the significant differences between FDA and PA surveillance radar, the scan time  $T_{sc}$  in the traditional definition is equal to  $T_r$ , since the intrapulse beam-scanning. It means more returned pulses from the target can be integrated in the same slow-time interval. This is at the price of lower directional gain in transmission. Other parameters are defined as follows.  $(SNR)_l$  is the minimum single-pulse SNR calculated by the Shnidman function,  $P_{av}$  is the average transmit power,  $G_r$  is antenna gain in a receiver,  $\lambda_0$  is the wavelength,  $\delta$  is the radar cross section (RCS) of a target,  $I(n_p)$  is the non-coherent integration gain,  $k$  is the Boltzmann constant,  $T_0$  is the equivalent noise temperature and  $F_n$  is the receiver noise coefficient.  $L_t$  is system loss and  $L_f$  is fluctuation loss.  $G_{id}(\Omega_{ROI})$  is calculated based on the predefined values of  $R_{id}$  in each ROI specifically. In the final stage, the sequential optimization can be implemented to solve (22).

## 4 Quantitative design of spatial allocation of observation bandwidth in coherent FDA radar

Due to the existence of frequency diversity gain [7–9], high range resolution radar takes the advantages not only in target identification but also in target detection. Based on coherent FDA, the spatial range resolution in different ROI can be further optimized by the allocation of transmit bandwidth. In this section, the quantitative design of observation bandwidth is provided based on wideband detection theory.

### 4.1 Determination of spatial observation bandwidth in coherent FDA radar

In existent literature, the practical observation bandwidth of coherent FDA radar has not been conclusively discussed, only a rough approximation is given as  $B' \approx B/M$  [39,40], which is not suitable in many cases. Consequently, the observation bandwidth of coherent FDA is analyzed at the beginning.

As discussed in Section 2, the intrapulse beam-scanning leads to the reduction of beam dwell time at a certain direction. It leads to the loss of integrated bandwidth when using FM waveform. Considering the angular velocity of beam-scanning is  $\omega_\theta = \partial \sin \theta / \partial t = \lambda_0 \Delta f / d$  and the 3-dB beamwidth is  $\theta_{\text{width}} \approx \lambda / D = 2 / (M - 1)$ , the beam dwell time of signal model in (17) at a certain direction is derived as

$$T_{s,l} = \frac{\theta_{\text{width}}}{\omega_{\theta_l}} \approx \frac{1}{(M-1)\Delta f_l}, \quad (24)$$

where an approximation of  $\sin(\theta_{\text{width}}) \approx \theta_{\text{width}}$  is introduced, because the beamwidth is relatively narrow.

Define  $f'(t)$  as the frequency modulating rate of the baseband waveform  $\varphi_l(t)$ , the practical observation bandwidth yields by fast-time integration as follows:

$$B_{s,l} = \int_{t_0}^{t_0+T_{s,l}} f'(t) dt \approx f'(t_0) \cdot T_{s,l}. \quad (25)$$

Considering  $\varphi_l(t)$  is an LFM signal with chirp rate  $f'(t) = \mu_l = B_l / T_{p,l}$ , the observation bandwidth in the  $l$ th angular sector is  $B_{s,l} = \mu_l T_{s,l} \approx \frac{B_l}{(M-1)\Delta f_l T_{p,l}}$ . Then, substituting  $\Delta f_l = \frac{\Theta_l}{2T_{p,l}}$  into the equation and the practical range resolution in the  $l$ th angular sector is derived as

$$\rho_l = \frac{c}{2B_{s,l}} = \frac{c \cdot (M-1)\Theta_l}{4B_l}. \quad (26)$$

Eq. (26) indicates that if it is intended to acquire expected range resolution  $\rho_l$  in  $\Omega_l$ , the bandwidth of LFM waveform in subpulse is required as  $B_l = \frac{c \cdot (M-1)\Theta_l}{4\rho_l}$ . It is important to note that the practical range resolution of coherent FDA is decreased only if the baseband waveform is FM. So far, the conclusive derivation of practical observation bandwidth and range resolution in coherent FDA are given in (25) and (26), which can be used to carry out the following analysis.

### 4.2 Quantitative design of optimal range resolution in target detection

Frequency diversity gain in wideband detection can be explained by Parseval's theorem, where the non-coherent summation of the target's range profile in the time domain is equivalent to integrate the energy of the target's frequency response in the frequency domain [8]. Nevertheless, the frequency diversity gain arises at the price of non-coherent loss. In consequence, with joint consideration of frequency diversity gain and non-coherent loss, the optimal range resolution dose exist at the "turning point" of SNR gain [9].

In this study, the frequency diversity gain is defined as the anti-fluctuation gain, which means the mitigation of fluctuation loss compared with the narrowband observation, where the target is located in a single range cell. The fluctuation loss is defined as the additional required SNR to achieve the same  $P_d$  and  $P_{\text{fa}}$  compared with the non-fluctuation target (Swirling 0) as follows:

$$L_f(\mathbf{\Gamma}, \text{SW}(i)) = \text{SNR}(\mathbf{\Gamma}, \text{SW}(i)) - \text{SNR}(\mathbf{\Gamma}, \text{SW}0), \quad (27)$$

where  $\mathbf{\Gamma} = \{P_d, P_{\text{fa}}, n_r\}$  is the set of parameters in detection. Note that  $n_r$  denotes the number of non-coherent integration samples and the number of range cells on target in detection. Based on the Swirling and Marcum model, the minimum required SNR( $\mathbf{\Gamma}, \text{SW}(i)$ ) can be calculated by iterative operation.

Since the detailed procedures have been provided in [41], no further elaboration is discussed in this paper.

Based on the definition above, the frequency diversity gain yields

$$[G_f]_{\text{dB}} = L_f(\mathbf{\Gamma}_1, \text{SW}(i)) - L_f(\mathbf{\Gamma}_{n_r}, \text{SW}(i)), \quad (28)$$

where  $L_f(\mathbf{\Gamma}_1, \text{SW}(i))$  and  $L_f(\mathbf{\Gamma}_{n_r}, \text{SW}(i))$  denote the fluctuation loss in narrowband and  $n_r$ -sampling wideband detection, respectively.

Then, non-coherent integration loss, which is defined as the additional SNR between the  $n_r$ -sampling coherent and non-coherent integration, is considered. As for a narrowband radar, the target is located in one range cell and its impulse response can be considered as a coherent integration of the target's range profile. Then, based on [36], the empirical  $n_r$ -sampling improve factor from the non-coherent integration is defined as

$$[I(n_r)]_{\text{dB}} = 6.79(1 + 0.253P_d) \left(1 + \frac{\log(1/P_{\text{fa}})}{46.6}\right) \log(n_r) \cdot \left[1 - 0.14 \log(n_r) + 0.01831(\log(n_r))^2\right]. \quad (29)$$

Consequently, the non-coherent integration loss yields

$$[L_{\text{NC}}]_{\text{dB}} = 10 \log(n_r) - [I(n_r)]_{\text{dB}}, \quad (30)$$

where  $10 \log(n_r)$  denotes the value of SNR gain in coherent integration.

In general consideration, the SNR gain acquired in wideband detection is the summation of frequency diversity gain and non-coherent integration loss, which can be expressed as

$$[G_{\text{SNR}}]_{\text{dB}} = -[L_{\text{NC}}]_{\text{dB}} + [G_f]_{\text{dB}}. \quad (31)$$

Assuming an interested target with 16 m in boresight, numerical simulations are presented to illustrate the proposed quantitative design of optimal range resolution.  $P_{\text{fa}} = 10^{-5}$  is assumed and the Swerling 1 to Swerling 4 cases are studied. SNR gain acquired in wideband detection as a function of different numbers of range cells on target are illustrated in Figure 4. Comparison of the entire SNR gain between Swerling 1/2 and Swerling 3/4 cases indicates that the target with strong fluctuation (Swerling 1/2) will acquire more frequency diversity gain in wideband detection than weak fluctuation target (Swerling 3/4). Furthermore, it also indicates that the SNR gain acquired from wideband observation has a positive relationship with the detection probability  $P_d$  (obviously, higher  $P_d$  means higher received SNR). When  $P_d = 0.95$ , the highest SNR gain reaches 7.189 dB in Figure 4(a) and 2.326 dB in Figure 4(b). By counting the turning points corresponding to different  $P_d$  values in Figure 4, the optimal numbers of range cells in wideband detection are illustrated in Figure 5. It is revealed that the optimal number of range cells arises with the increase of SNR (represented by  $P_d$  in Figure 5). When  $P_d$  reaches 0.99, the optimal  $n_r$  of Swerling 1/2 and Swerling 3/4 arise to 12 and 5, respectively. Based on the fitting curves, the optimal number of range cells on target  $n'_r$  can be determined and the optimal detection bandwidth yields (under the assumption of LFM waveform)

$$B'_l = \frac{c \cdot (M - 1) \Theta_l n'_r}{4l_t}, \quad (32)$$

where  $l_t$  is the target length in boresight.

According to the aforementioned analysis, the optimal detection bandwidth can be estimated with the prior knowledge of the target's length and Swerling types. This information is usually attainable for targets of interest in different ROI. Consequently, based on the multiscale observation ability of coherent FDA radar, the optimized spatial bandwidth allocation can be implemented. Although the rigorous optimal frequency diversity gain is hard to realize in practice, the quantitative calculation provided in this section is still meaningful to acquire better detection performance. It also needs to be attention that the wideband observation discussed in this section means discriminating the target into more than one range unit. It has a different meaning from the typical definition of wideband signal and it does not conflict with the narrowband assumption in Section 2.

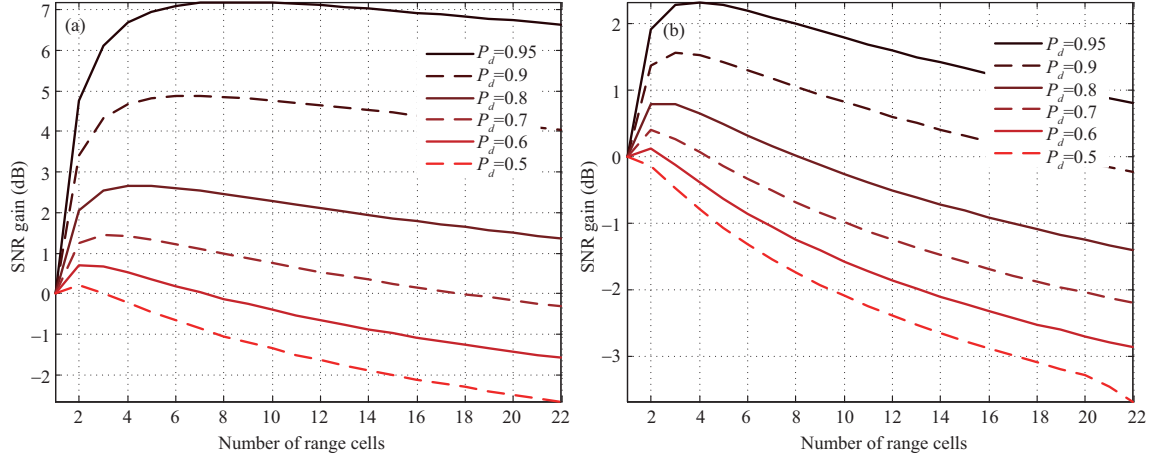


**Figure 4** SNR gain changing with the number of range cells on target. (a) Swerling 1/2; (b) Swerling 3/4.

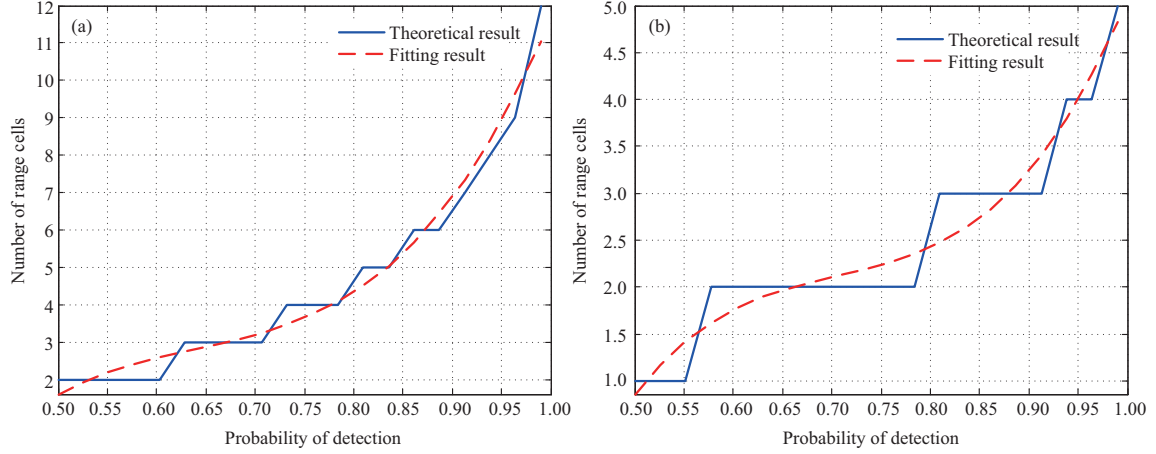


**Figure 5** Optimal number of range cells on target in detection changing with  $P_d$ . (a) Swerling 1/2; (b) Swerling 3/4.

### 4.3 Complete process of the multiscale observation method based on coherent FDA

Jointly considering the discussions in the above sections (including spatial waveform diversity, quantitative design of beampattern, and observation bandwidth), the proposed method opens the way to achieve multiscale observation in wide-spatial radar surveillance. We assume that the maximum transmit bandwidth is defined as  $B_t = \sum_{l=1}^L B_l$ . Then, the complete implementations of the proposed method are given in Algorithm 1.

## 5 Numerical simulations and results

This section validates the effectiveness of the proposed multiscale observation and waveform selection principles in coherent FDA, as well as the quantitative beampattern synthesis, spatial waveform, and bandwidth diversity. The system parameters according to a ground-based collocated FDA radar constituted by ULA are provided in Table 1. The idealized non-directional elements are assumed (the directional gain of every single element is 0 dB), and the antenna gain is calculated based on array pattern synthesis.

### 5.1 Multidimensional AF and comparative simulations between different radar systems

The AF is an effective tool that can be used to analyze the waveform characteristics, including the range resolution, Doppler tolerance, and sidelobe performance. However, it is difficult to evaluate the spatial diverse waveforms using the traditional AF due to the lack of angular resolution. Consequently, inspired

---

**Algorithm 1** Quantitative design of multiscale observation in wide-spatial FDA radar surveillance
 

---

**Input:** Specialized ROI  $\Omega_{\text{ROI}} = \{\Omega_1, \Omega_2, \dots, \Omega_K\}$ . Prior knowledge of the interested target, including Swerling type and target's length. Requirements in detection, including  $P_d, P_{fa}$ . Radar system parameters in (23). Required beampattern gain  $G_{\text{id}}(\Omega_{\text{ROI}})$  or detectable range extension  $R_{\text{id}}(\Omega_{\text{ROI}})$ .

**Output:** Designed signals for  $M$  transmit elements  $[s_1(t), s_2(t), \dots, s_M(t)]$ .

**Step 1.** Calculate the minimum detectable  $(\text{SNR})_l$  by Shnidman function based on the requirements in detection and the prior knowledge of interested target;

**Step 2.** Determine the required beampattern gain  $G_{\text{id}}(\Omega_{\text{ROI}})$  directly or calculate from (23) with the predefined range extension  $R_{\text{id}}(\Omega_{\text{ROI}})$ ;

**for**  $k = 1 : K$  **do**

**for**  $T_{p,k}$  in  $[T_{s,k}, T_{s,k} + \Delta_T, \dots, T_p]$  **do**

        1. Sequentially calculate the cost function in (22) with searching step  $\Delta_T$  in the searching range  $[T_{s,k}, T_p]$ ;

        2. Locate the minimum value of the cost function and record the corresponding subpulse duration as  $\hat{T}_{p,k}$ ;

**end for**

        3. Calculate the optimal observation bandwidth  $B'_k$  by (32) with prior knowledge assistance;

**end for**

**Step 3.** Baseband waveforms  $\{\varphi_1(t), \varphi_2(t), \dots, \varphi_L(t)\}$  in  $L$  subpulses are designed with the consideration of observed environments in different angular sectors;

**Step 4.** Calculate the time-shifts  $\eta_l$  and frequency offsets  $\Delta f_l$  based on (18) and (19). Finally, integrate the subpulse waveforms by (17) and feed the synthesized signal to transmit elements.

---

**Table 1** Coherent FDA radar parameters in simulation

Parameter	Symbol	Value
Reference frequency	$f_0$	10 GHz
Total bandwidth	$B_t$	500 MHz
Pulse duration	$T_p$	10 $\mu$ s
Average power of transmitter	$P_{av}$	400 W
Pulse repetition time	$T_r$	5 ms
System loss	$L_t$	15 dB
Receiver noise coefficient	$F_n$	3 dB
Receive antenna gain	$G_r$	33.94 dB
Number of transmit elements	$M$	20
Number of receive elements	$N$	50
Range of surveillance	$\Omega$	$[-90^\circ, 90^\circ]$

---

by the space-time matched filter in (10), the multidimensional AF is developed as follows:

$$|\chi(\tau, f_d, \theta, \theta')|^2 = \left| \sum_{n=1}^M \sum_{m=1}^M e^{j(\mathbf{k}^T(\theta)\mathbf{x}(m) - \mathbf{k}^T(\theta')\mathbf{x}(n))} \cdot \int_{-\infty}^{+\infty} s_m(t) s_n^*(t - \tau) \cdot e^{j2\pi f_d t} dt \right|^2, \quad (33)$$

where  $\mathbf{k}(\theta) = \frac{2\pi \sin \theta}{\lambda_0} \mathbf{e}_k$  is the wavenumber vector and  $\mathbf{x}(m) = (m-1)d \cdot \mathbf{e}_x$  is the relative position vector.  $\theta$  represents the direction of received signal and  $\theta'$  represents the direction of spatial filtering.

The multidimensional AF is equivalent to the received signal processing of a multi-input single-output system. The equivalent beamforming is operated in conjunction with pulse compression. Because the  $|\chi(\tau, f_d, \theta, \theta')|^2$  is a four-dimensional function, its bi-dimensional expressions are usually applied to present the visualized results.  $\chi(\tau, f_d; \theta = \theta')$  is the range-Doppler AF, which is utilized to evaluate the range correlation and Doppler tolerance.  $\chi(\theta, \theta'; \tau = 0, f_d = 0)$  denotes the bi-dimensional angular AF, which illustrates the spatial coverage and angular resolution in transmission.  $\chi(\tau, \theta; \theta' = \theta_0, f_d = 0)$  represents the range-angle AF, which evaluates the angular and range focusing performance according to the equivalent beamforming direction  $\theta_0$ . In the following simulations, the multidimensional AFs are utilized to analyze the performance of the proposed method.

First, the bi-dimensional angular AF is applied to demonstrate the spatial coverage performance and establish a quantitative analysis of the relative gain in transmission. Based on the system parameters highlighted in Table 1, bi-dimensional angular AFs of PA radar, orthogonal MIMO, and coherent FDA are demonstrated in Figure 6. Observations of the diagonal of bi-dimensional angular AFs reveal that the PA radar cannot achieve complete spatial coverage. In comparison, both the MIMO and FDA radar yield high transmitting gain when  $\theta = \theta' \in [-90^\circ, 90^\circ]$ . Compared to coherent FDA, the spatial distribution of transmitting gain in orthogonal MIMO is not uniform because it is difficult to generate the strictly orthogonal waveform in practical applications.

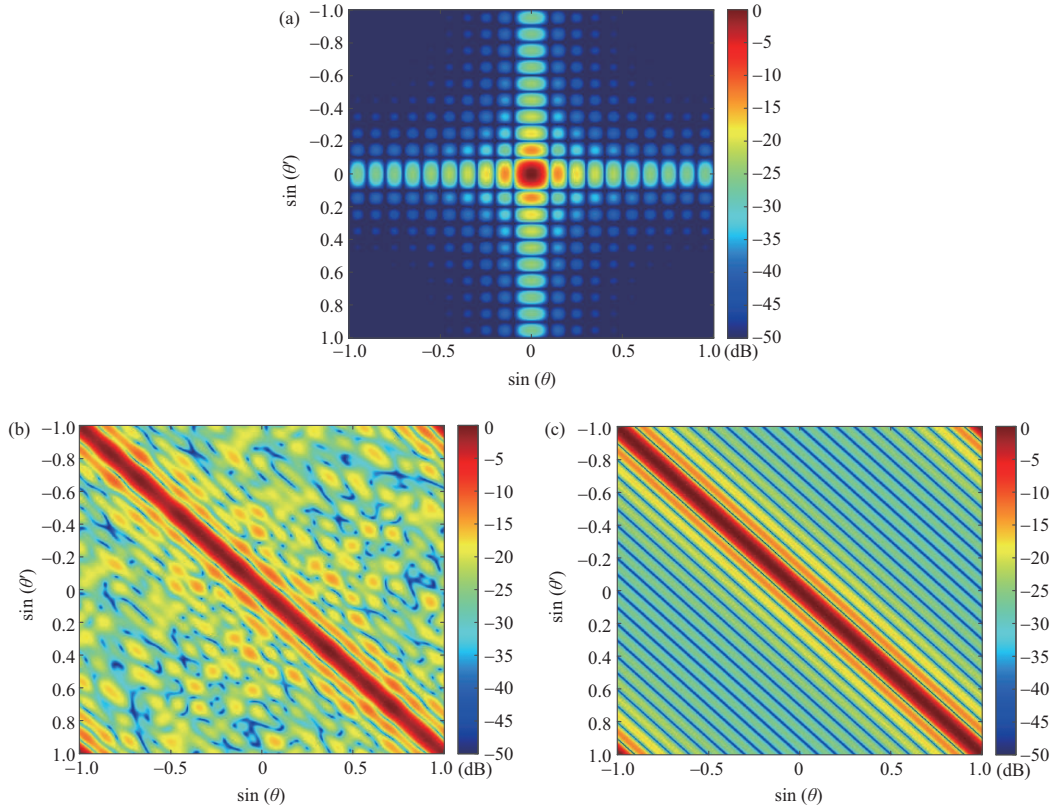


**Figure 6** Bi-dimensional angular AFs of different radar systems. (a) PA; (b) orthogonal MIMO; (c) coherent FDA.

## 5.2 Validation of spatial waveform diversity

To validate the spatial waveform diversity, the first simulation is conducted by dividing the entire observation field into three angular regions:  $\Omega_1 = [30^\circ, 90^\circ]$ ,  $\Omega_2 = [-30^\circ, 30^\circ]$ , and  $\Omega_3 = [-30^\circ, -90^\circ]$ . For these angular sectors, different types of subpulse waveforms are designed. The time-frequency diagram of the transmit baseband waveform is displayed in Figure 7. As demonstrated previously, an LFM waveform is designed for  $\Omega_1$ , a tangent FM waveform is designed for  $\Omega_2$ , and a phase-coded waveform with a  $-40$  dB sidelobe level is designed for  $\Omega_3$ . The subpulse durations are calculated by  $T_{p,l} = \Theta_l/2\Delta f$ . To realize full-spatial coverage,  $\Delta f = 1/T_p$  is assumed. Consequently,  $T_{p,1} = 2.5 \mu\text{s}$ ,  $T_{p,2} = 5 \mu\text{s}$ , and  $T_{p,3} = 2.5 \mu\text{s}$ . The code length of phase-coded waveform is set to  $n_c = 120$  and the code width yields  $t_b = T_{p,3}/n_c \approx 0.021 \mu\text{s}$ , corresponds to  $B_3 = 48$  MHz. The bandwidth of LFM and Tangent FM signals are set to  $B_1 = B_2 = 0.5(B_t - B_3) = 226$  MHz.

Furthermore, the range-angle AF is adopted to evaluate the properties of the received signal from three equivalent transmit DBF directions. In this simulation, the equivalent beamforming is implemented by setting  $\theta' = 40^\circ$ ,  $\theta' = 0^\circ$ , and  $\theta' = -40^\circ$  in (33), respectively. The three different range-angle AFs are demonstrated in Figures 8(a)–(c). Detailed illustrations in red dashed squares are placed at the left corner of subfigures, and a comparison of centered range profiles in these three directions is shown in Figure 8(d). From Figures 8(a)–(c), it is evident that different impulse responses are acquired when equivalent boresight varies from  $\Omega_1$  to  $\Omega_3$ . In Figure 8(a), the sidelobe clutter appears as a result of the high pedestal of the phase-coded waveform. In contrast, when the boresight is aimed at  $\theta' = 0^\circ$  and  $\theta' = -40^\circ$ , the coupled energy from the phase-coded waveform in the third subpulse is suppressed by the space-time windowing effect of the FDA beampattern. Thus, the sidelobe clutters are substantially mitigated, as shown in Figures 8 (b) and (c).

A comparison of the range profiles in three directions is illustrated in Figure 8(d). When  $\theta' = 40^\circ$  corresponding to LFM waveform in the first subpulse, the 3-dB range resolution is 3.05 m, which is coincident with the theoretical value  $\rho_l = \frac{c(M-1)\Theta_l}{4B_l} = 3.15$  m. When the boresight aims at  $\theta' = 0^\circ$ , the practical range resolution of Tangent FM signal is 10.5 m, and the theoretical range resolution, which is calculated according to (25), is 11.25 m, which are also coincident. For the received phase-coded signal

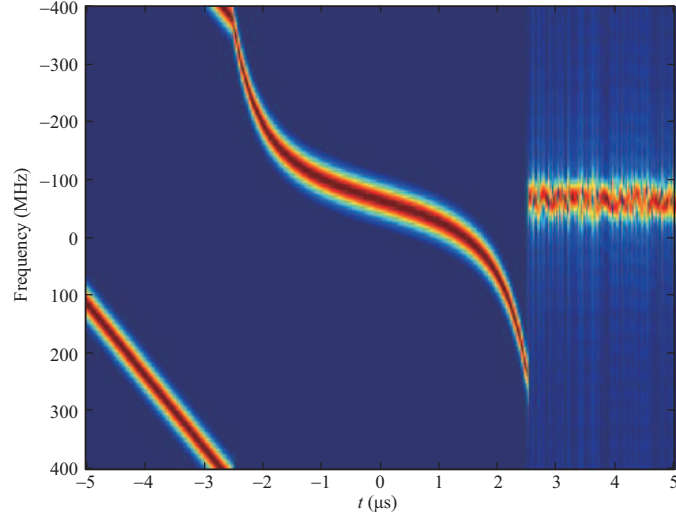


Figure 7 Time-frequency diagram of transmit baseband waveform.

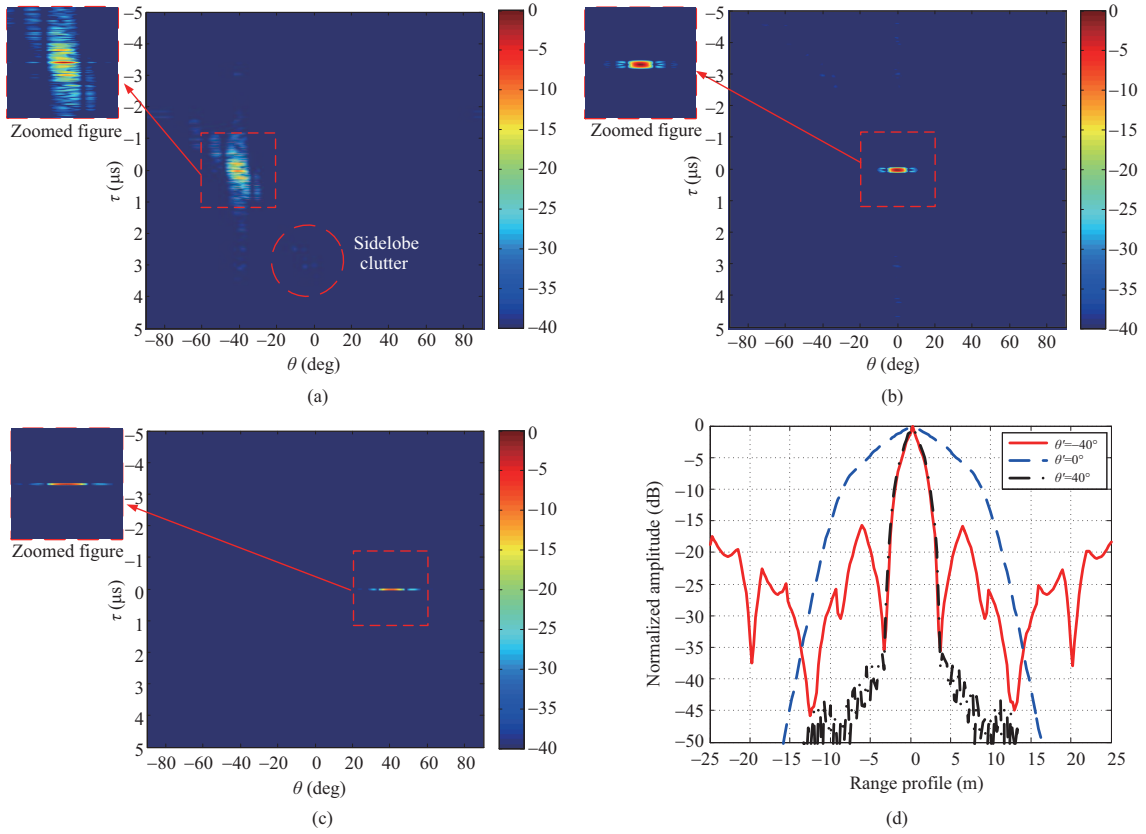


Figure 8 Range-angle AFs with different beamforming directions and the comparison of one-dimensional range profiles. (a) Boresight aiming at  $\theta' = -40^\circ$ ; (b) boresight aiming at  $\theta' = 0^\circ$ ; (c) boresight aiming at  $\theta' = 40^\circ$ ; (d) comparison of range profiles in these directions.

from  $\theta' = -40^\circ$ , the measured range resolution is 2.85 m, slightly surpassing its theoretical value, which is 3.125 m. The range resolution of the phase-coded waveform, which is  $-15.41$  dB, is enhanced with the PSLR elevation. The PSLR aggravation of phase-coded waveform in coherent FDA radar is induced as a result of the cross terms ( $m \neq n$ ) in (11). The PSLRs of the LFM and Tangent FM waveforms correspond to  $-35.99$  and  $-61.49$  dB, respectively. The remarkable improvement in the PSLR of FM waveforms in coherent FDA radar may be attributed to the range shift of cross terms in (11). The simulation results in Figure 8 validate the principles of waveform selection proposed in Section 2 quantitatively.

**Table 2** Simulation parameters in this subsection

Parameter	Symbol	Value
Detection probability	$P_d$	0.9
False-alarm probability	$P_{fa}$	$10^{-6}$
RCS of interested target	$\delta$	$10 \text{ m}^2$
Number of integration pulses	$n_p$	30
Non-coherent integration gain	$I(n_p)$	11.58 dB
Fluctuation loss	$L_f(\Gamma, SW(i))$	1.74 dB
Detectable single-pulse SNR	$(SNR)_l$	21.35 dB

### 5.3 Validation of quantitative beampattern synthesis and detectable range extension

In this subsection, the quantitative beampattern synthesis and detectable range extension in specialized ROI are presented. The two spatial distinct ROI are designed as  $\Omega_{ROI} = \{[-20^\circ, 0^\circ], [30^\circ, 50^\circ]\}$ . The interested target is assumed as a jet aircraft, which is a typical Swerling 2 target, and the related parameters used in this simulation are demonstrated in Table 2.

The coherent gain of FDA radar in the receiver is equivalent to the PA radar, given that the coherent synthesis in the received array is the same in these modes. However, the coherent gain of FDA in transmit is considerably different from PA or orthogonal MIMO radar. Due to the intrapulse beam agility, the coherent gain of FDA in transmit should be calculated by (20) for quantitative analysis. According to the system parameters, the lower bound of beampattern gain  $G_l = 6.88$  dB is derived when  $\Delta f = 1/T_p$  (used as a reference), and the upper bound of beampattern gain  $G_u = 26.01$  dB is derived in the PA mode. Therefore, the designable range of beampattern gain is  $|G_u - G_l| = 19.13$  dB. Then, based on the surveillance radar equation in (23), the lower and upper bounds of the detectable range are calculated as  $R_l = 13.24$  km and  $R_u = 39.81$  km. In the following simulation, the idealized range extensions  $\Delta R = R_{id} - R_l$  in ROI are set as 2, 4, 6, and 8 km. According to (23), the required additional beampattern gain  $\Delta G = G_{id}(\Omega_{ROI}) - G_l$  is 2.44, 4.58, 6.49, and 8.22 dB, respectively. Another example may be presented by setting  $\Delta R_1 = 8$  km in  $[-20^\circ, 0^\circ]$  and  $\Delta R_2 = 2$  km in  $[30^\circ, 50^\circ]$ , which demonstrates the ability to synthesize different beampattern gain in different ROI. Qualitative illustrations of bi-dimensional angular AFs are presented in Figure 9, and quantitative comparisons are carried out based on one-dimensional equivalent beampattern defined by (20) in Figure 10.

From the diagonal of angular AFs in Figure 9, the transmit beampattern gain in specialized ROI is gradually strengthened as the predefined range extensions are increased. Furthermore, as is illustrated in Figure 10, when the detectable range extension  $[\Delta R_1, \Delta R_2]$  increases from 2 to 8 km, the maximum beampattern gain increases from 2.46 to 8.23 dB in  $[-20^\circ, 0^\circ]$  and from 2.47 to 6.50 dB in  $[30^\circ, 50^\circ]$ , respectively. The simulation result in Figure 10 validates the feasibility of the proposed method to synthesize the required beampattern gain precisely according to the predefined range extension. The slight between the two ROIs is induced by the non-linear relationship between degrees and sines (although the beam-scanning velocity is constant in sinusoidal form, it will be nonlinearly transformed into degree form). Considering the uninterested angular sectors, the maximum beampattern loss is  $-8.55$  dB, which corresponds to  $\Delta R_1 = \Delta R_2 = 6$  km. In the case of  $\Delta R_1 = \Delta R_2 = 2$  km, the maximum beampattern loss is  $-1.75$  dB. This means the additional beampattern gain in ROI is traded by the loss of illumination time in uninterested angular sectors. Furthermore, compared to the beampattern designed by existing studies in [21], the proposed method capitalizes on the additional DOF, and this further helps quantitatively design the beampattern gain in ROI.

### 5.4 Validation of frequency diversity gain and quantitative design in spatial bandwidth allocation

In this subsection, the frequency diversity gain in wideband detection and the proposed quantitative design of spatial bandwidth allocation are validated based on real-measured data. The high range resolution profiles (HRRP) of an airbus A320 in flight are measured at Hefei airport by a wideband monostatic radar with 200 MHz bandwidth, 250 MHz sampling rate and carrier frequency at  $f_0 = 15.5$  GHz. The target length in boresight is 24 m, and the average received signal SNR per sample is 7.2 dB (estimated from the HRRP). The narrowband range profiles are generated by sub-band decomposition, and the energy loss in spectrum split is recovered by non-coherent integration between adjacent pulses. The real-measured

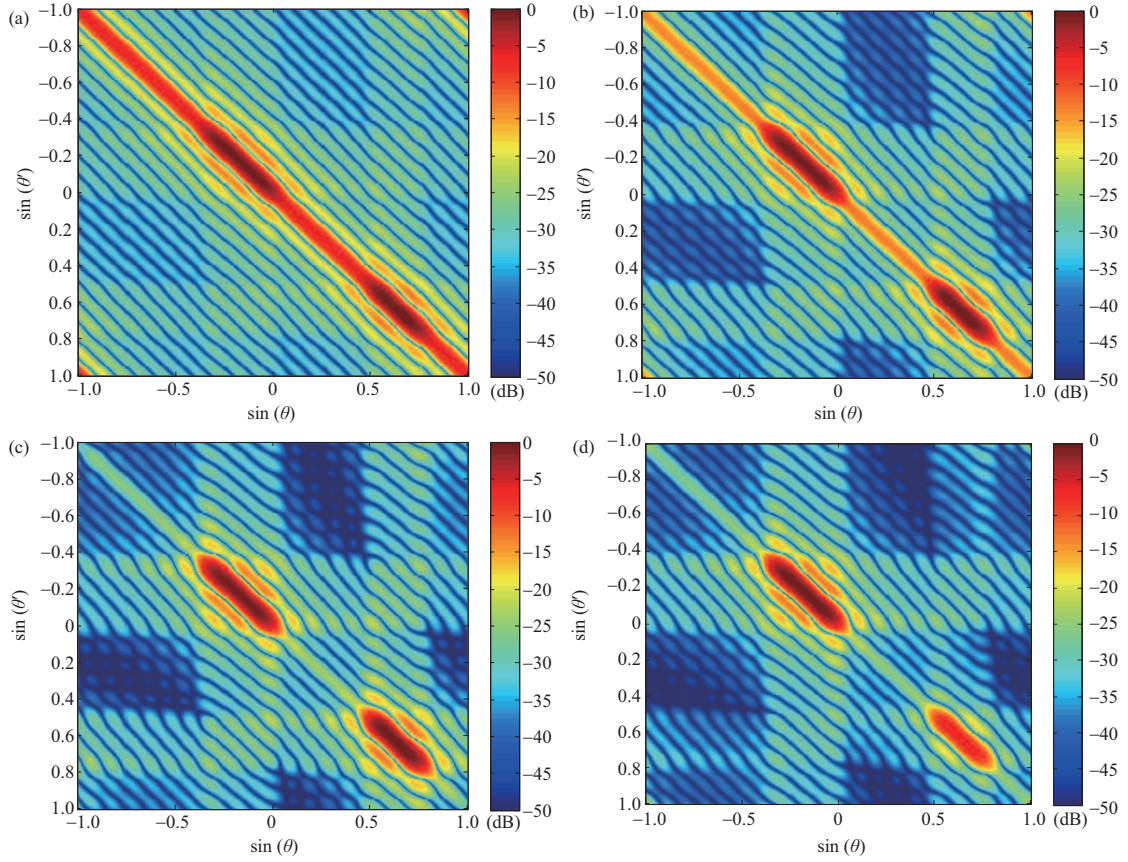


**Figure 9** Bi-dimensional angular AFs with range extensions in  $[-20^\circ, 0^\circ]$  and  $[30^\circ, 50^\circ]$ . (a)  $\Delta R = 2$  km; (b)  $\Delta R = 4$  km; (c)  $\Delta R = 6$  km; (d)  $\Delta R_1 = 8$  km in  $[-20^\circ, 0^\circ]$  and  $\Delta R_2 = 2$  km in  $[30^\circ, 50^\circ]$ .

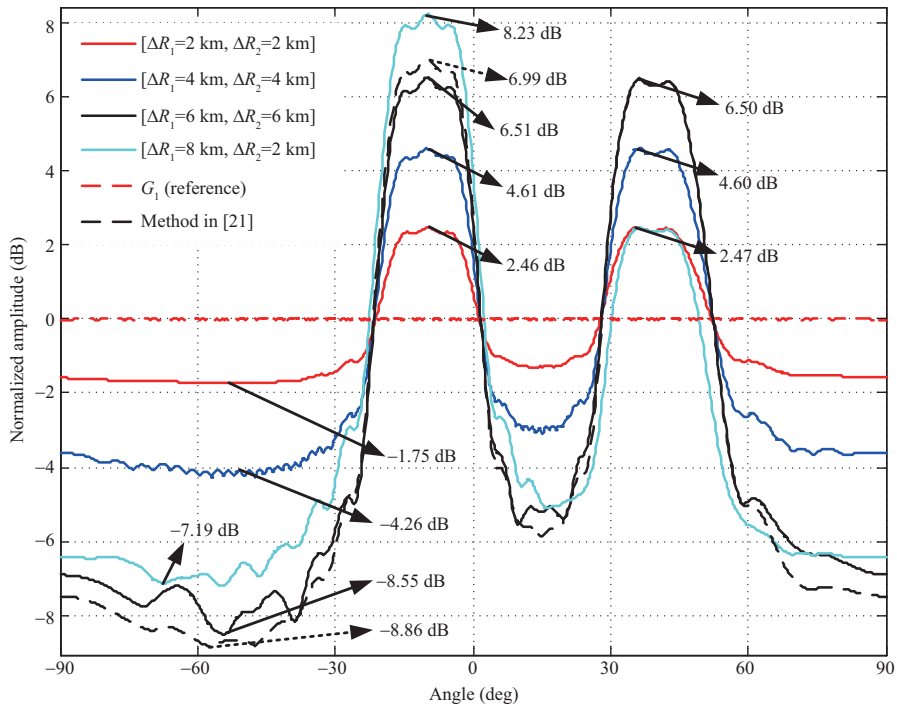


**Figure 10** Comparison of the one-dimensional equivalent beampatterns.

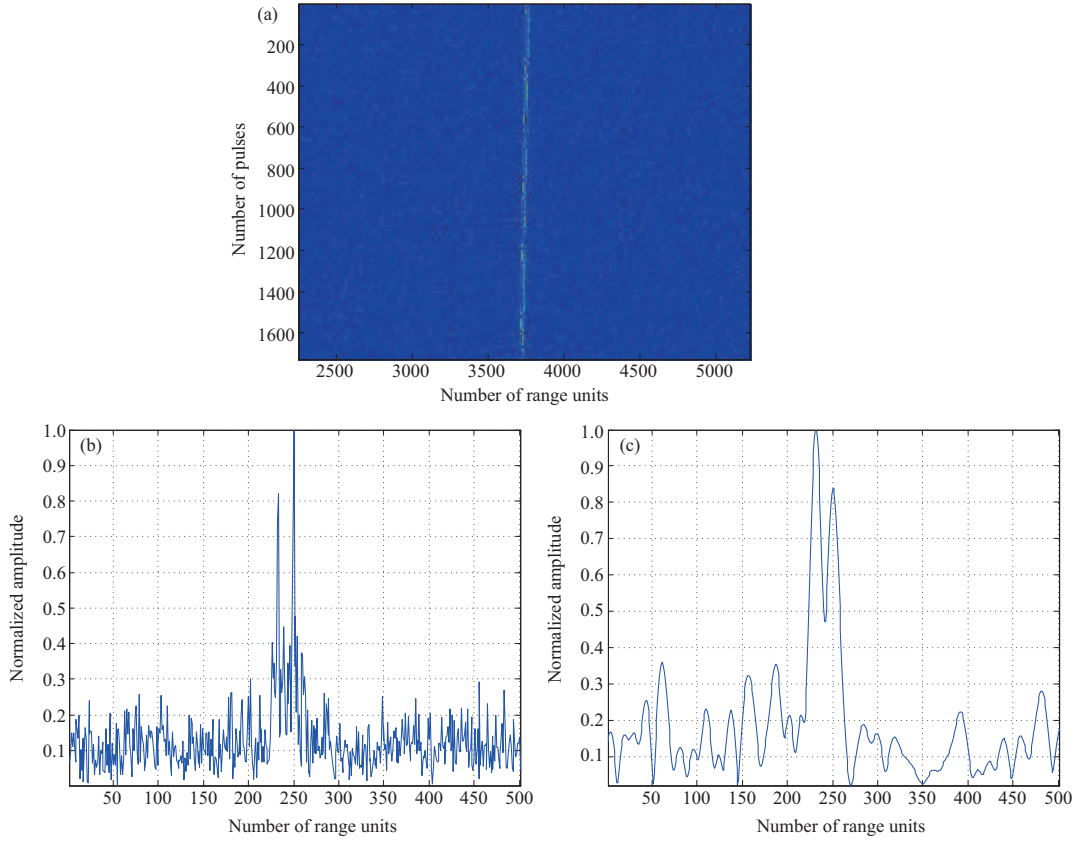


**Figure 11** Real-measured HRRP data of an airbus A320 in flight. (a) Part of raw data; (b) HRRP with a range resolution of 0.75 m; (c) narrowband profiles with a range resolution of 7.5 m.

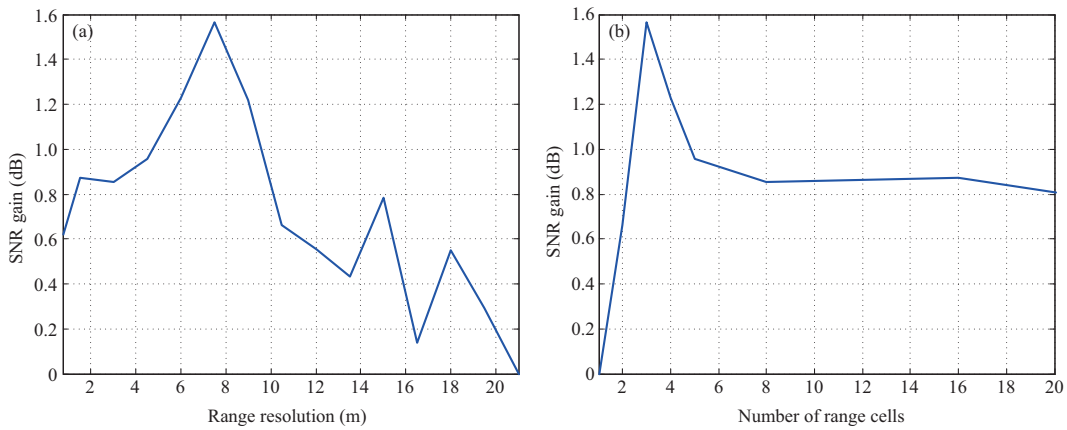


**Figure 12** Illustration of SNR gain in wideband detection. (a) Change in SNR gain according to range resolution; (b) change in SNR gain according to the number of range cells on target.

raw data, HRRP, and narrowband range profiles are demonstrated in Figure 11.

Because the airplane has a linear radial velocity (about  $64 \text{ m} \cdot \text{s}^{-1}$ ), the envelope alignment is introduced at the beginning for convenient extraction of the target’s energy in different pulses. The multiscale sub-band decomposition is introduced to generate the narrowband range profiles corresponding to different range resolutions. In this simulation, we set the range resolution as 0.75–21 m, and the average SNR gain (compared with the narrowband case) in different situations is derived by performing Monte-Carlo experiments for a total of 500 times. The curves of SNR gain change according to the range resolution, and the number of range cells on target is demonstrated in Figure 12.

In Figure 12, it is briefly illustrated that the optimal detection range resolution in this data is 7.5 m, and the optimal number of range cells on target is three. The maximum SNR gain acquired from frequency

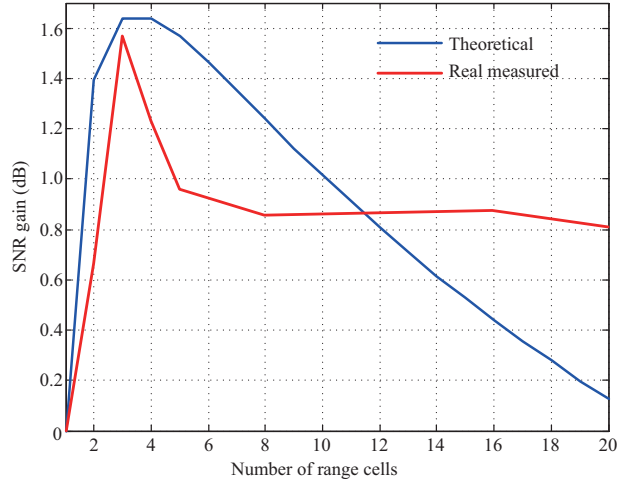


**Figure 13** Theoretical analysis of change in SNR gain according to the number of range cells on target.

diversity gain is 1.57 dB. To validate the feasibility of theoretical analysis, the quantitative design of optimal detection bandwidth proposed in Section 4 is presented. Based on the CFAR detection with  $P_{fa} = 10^{-5}$  on this dataset, the single-pulse detection probability is approximately 0.72. Based on prior knowledge, the jet aircraft, like airbus A320, is a typical Swerling 2 target. The theoretical curve of the change in SNR gain according to the number of range cells on target is derived using the method proposed in Section 4, as demonstrated in Figure 13 and compared with the real-measured curves in Figure 12(b). It is illustrated that the optimal number of range cells in theoretical is three, and the maximum SNR gain is 1.64 dB, which is in agreement with the experiment results. Further, it can be seen that the theoretical curve of SNR gain is consistent with the result in Figure 12(b). The comparison between experimental and theoretical curves validates the effectiveness of the proposed quantitative bandwidth allocation method.

In summary, the experiments on real-measured datasets validate the presence of frequency diversity gain and optimal detection range resolution. Consequently, based on prior knowledge of interested targets, the quantitative results derived from this subsection can be used to carry out the spatial bandwidth allocation in coherent FDA multiscale observation for better detection performance. It should be noted that the quantitative design of observation bandwidth can be used not only in coherent FDA systems but also in other radar applications with sufficient observation bandwidth.

## 6 Discussion

In this section, we discuss the relationship between this work and the concept of computational array [4], and we further present two detailed strategies, which will help reduce the computational burden and subsequently improve the practicality of the proposed method.

First, the idea of the computational array is proposed by integrating the sensing and computing, especially the unit computing. In that framework, a three-level computing architecture of “element-module-system” is established. One of the primary benefits of the computational array is the high transmit freedom [4]. Thus, the proposed multiscale observation of coherent FDA radar can be regarded as a preliminary attempt of the computational array. In the first place, the high transmit DOFs of coherent FDA are in conjunction with the computational array. Furthermore, the unit computation can be driven by coherent FDA radar due to the beam-scanning properties. Finally, because the transmit directivity can be reconstructed by only one receive unit, the coarse-accuracy information can be acquired from a single receive unit. By integrating all receiving units, the high-accuracy information can be extracted, which corresponds to the “element-module-system” architecture.

Second, as discussed in Section 4, the practical observation bandwidth  $B_{s,l}$  in the  $l$ th angular sector is less than the baseband waveform bandwidth in the  $l$ th subpulse. As illustrated in (25), the practical observation bandwidth is determined by beam dwell time and frequency modulating rate. Consequently, adjustable sampling rates can be applied in the receiver, and it is not necessary to maintain high sampling rates in all directions. For example, when dealing with the received signal from the  $l$ th angular sector (by

receiving DBF), the sampling rate can be set as  $F_s^l \geq B_{s,l}$ , rather than  $B_l$  or  $B_t$ . For the same reason, the bandwidth of the receiver can also be saved to mitigate the power spectrum of thermal noise, and the constraint is  $B_{IF} > \max\{B_{s,1}, B_{s,1}, \dots, B_{s,L}\}$ .

Last, the frequency offset between adjacent elements in coherent FDA can be included in the transmit baseband waveform (for example, adding a constant frequency term in the transmitted signal) because the variation of frequency offsets is relatively small. Considering an excessive condition, where  $\Theta_l = |\sin(90^\circ) - \sin(-90^\circ)| = 2$ , and the subpulse duration  $T_{p,l}$  varies from 0.1 to 100  $\mu\text{s}$ , the variation range of  $\Delta f_l$  is only 0.01–10 MHz. Thus, only a full-digital array with programmable transmitting channels possesses the ability to realize the proposed multiscale observation method in practice.

## 7 Conclusion

To deal with different targets from complex clutter and interference environments, wide-spatial surveillance radar necessitates the multiscale observation ability, which subsequently leads to improved performance. However, it is difficult to achieve this in conventional wide-coverage radar systems such as the ubiquitous radar and orthogonal MIMO radar system mainly due to the inadequate transmitting agility. Thus, a quantitative multiscale observation strategy is proposed for wide-spatial surveillance based on coherent FDA radar. Further, the realization of spatial waveform diversity and principles of waveform selection in coherent FDA are presented. Furthermore, the quantitative design of beam pattern gain in distinct ROI is developed and applied in detectable range extension. Further, the conclusive derivation of FDA observation bandwidth and the quantitative spatial bandwidth allocation are also proposed for better performance in detection. Last, this work can be regarded as an initial attempt of the computational array, which is an epochmaking concept. The numerical simulations indicate that with the ability of multiscale observation, the proposed method provides an opportunity to attain enhanced performance in wide-spatial surveillance and further indicates a huge potential for use in other applications.

**Acknowledgements** This work was supported by National Natural Science Foundation of China (Grant Nos. 62271495, 42205142, 62101561). The author would like to thank Dr. Qilei ZHANG for providing the real measured wideband data acquired in Hefei international airport.

## References

- 1 Drabowitch S, Aubry C. Pattern compression by space-time binary coding of an array antenna. In: Proceedings of the AGARD CP 66, Advanced Radar Systems, 1969
- 2 Chevalier F L. Space-time transmission and coding for airborne radars. *CIE J Radar Sci Technol*, 2008, 6: 411–421
- 3 Le Chevalier F. Space-time coding for active antenna systems. In: Principles of Modern Radar (Vol 2): Advanced Techniques. Stevenage Herts: SciTech Publishing, 2013
- 4 Wu M Q, Zhao Y, He F, et al. Computational array — digital array with computational empowerment (in Chinese). *Sci Sin Inform*, 2022, 52: 2270–2289
- 5 Chevalier F L, Savy L. Colored transmission for radar active antenna. In: Proceedings of the International Conference on Radar Systems RADAR, Toulouse, 2004
- 6 de Maio A, Lops M, Venturino L. Diversity-integration tradeoffs in MIMO detection. *IEEE Trans Signal Process*, 2008, 56: 5051–5061
- 7 Conte E, de Maio A, Ricci G. GLRT-based adaptive detection algorithms for range-spread targets. *IEEE Trans Signal Process*, 2002, 49: 1336–1348
- 8 Le Chevalier F, Petrov N. Diversity considerations in wideband radar detection of migrating targets in clutter. *Sci China Inf Sci*, 2019, 62: 040302
- 9 Shen M, He F, Dong Z, et al. Frequency diversity gain of a wideband radar signal. *Remote Sens*, 2021, 13: 4885
- 10 Kanter I. Exact detection probability for partially correlated rayleigh targets. *IEEE Trans Aerosp Electron Syst*, 1986, 22: 184–196
- 11 Dai F. Wideband radar signal processing — detection, clutter suppression and cognitive tracking (in Chinese). Dissertation for Ph.D. Degree. Xi'an: Xidian University, 2010
- 12 Li T. Study on some issues of wideband radar detection (in Chinese). Dissertation for Ph.D. Degree. Xi'an: Xidian University, 2011
- 13 Skolnik M. Attributes of the ubiquitous phased array radar. In: Proceedings of the IEEE International Symposium on Phased Array Systems and Technology, Boston, 2003. 101–106
- 14 de Quevedo A D, Urzaiz F I, Menoyo J G, et al. Drone detection and RCS measurements with ubiquitous radar. In: Proceedings of the International Conference on Radar, Brisbane, 2018. 1–6
- 15 Yu L, He F, Zhang Q L, et al. High maneuvering target long-time coherent integration and motion parameters estimation based on Bayesian compressive sensing. *IEEE Trans Aerosp Electron Syst*, 2023, 59: 4984–4999
- 16 Li J, Stoica P. MIMO radar with colocated antennas. *IEEE Signal Process Mag*, 2007, 24: 106–114
- 17 Ahmed S, Thompson J S, Petillot Y R, et al. Unconstrained synthesis of covariance matrix for MIMO radar transmit beam pattern. *IEEE Trans Signal Process*, 2011, 59: 3837–3849
- 18 Ahmed S, Thompson J S, Petillot Y R, et al. Finite alphabet constant-envelope waveform design for MIMO radar. *IEEE Trans Signal Process*, 2011, 59: 5326–5337
- 19 Gong P C, Shao Z H, Tu G P, et al. Transmit beam pattern design based on convex optimization for MIMO radar systems. *Signal Process*, 2014, 94: 195–201
- 20 He Z S, Li J, Liu H M, et al. Principles of colocated MIMO radar (in Chinese). In: MIMO Radar (Vol 1). Beijing: Nation Defense Industry Press, 2017
- 21 Wang H K, Liao G S, Xu J W, et al. Transmit beam pattern design for coherent FDA by piecewise LFM waveform. *Signal Process*, 2019, 161: 14–24

- 22 Antonik P, Wicks M C, Griffiths H D, et al. Frequency diverse array radars. In: Proceedings of the IEEE Conference on Radar, Verona, 2006. 1–3
- 23 Babur G, Aubry P, Le Chevalier F. Space-time radar waveforms: circulating codes. *J Electrical Comput Eng*, 2013, 2013: 1–8
- 24 Xu J W, Lan L, Zhu S Q, et al. Design of matched filter for coherent FDA radar. *Syst Eng Electron*, 2018, 40: 9
- 25 Wang W Q. Range-angle dependent transmit beampattern synthesis for linear frequency diverse arrays. *IEEE Trans Antennas Propagat*, 2013, 61: 4073–4081
- 26 Xu J W, Liao G S, Zhu S Q, et al. Joint range and angle estimation using MIMO radar with frequency diverse array. *IEEE Trans Signal Process*, 2015, 63: 3396–3410
- 27 Lan L, Rosamilia M, Aubry A, et al. Single-snapshot angle and incremental range estimation for FDA-MIMO radar. *IEEE Trans Aerosp Electron Syst*, 2021, 57: 3705–3718
- 28 Xu J W, Zhu S Q, Liao G S. Range ambiguous clutter suppression for airborne FDA-STAP radar. *IEEE J Sel Top Signal Process*, 2015, 9: 1620–1631
- 29 Xu J W, Liao G S, So H C. Space-time adaptive processing with vertical frequency diverse array for range-ambiguous clutter suppression. *IEEE Trans Geosci Remote Sens*, 2016, 54: 5352–5364
- 30 Lan L, Xu J W, Liao G S, et al. Suppression of mainbeam deceptive jammer with FDA-MIMO radar. *IEEE Trans Veh Technol*, 2020, 69: 11584–11598
- 31 Lan L, Liao G S, Xu J W, et al. Mainlobe deceptive jammer suppression using element-pulse coding with MIMO radar. *Signal Process*, 2021, 182: 107955
- 32 Lan L, Marino A, Aubry A, et al. GLRT-based adaptive target detection in FDA-MIMO radar. *IEEE Trans Aerosp Electron Syst*, 2020, 57: 597–613
- 33 Yu L, He F, Su Y, et al. Transmitting strategy with high degrees of freedom for pulsed-coherent FDA radar. *IET Radar Sonar Navi*, 2022, 16: 659–667
- 34 Lan L, Liao G S, Xu J W, et al. Range-angle-dependent beamforming for FDA-MIMO radar using oblique projection. *Sci China Inf Sci*, 2022, 65: 152305
- 35 Zeng L, Zhang Z J, Wang Y L, et al. Suppression of dense false target jamming for stepped frequency radar in slow time domain. *Sci China Inf Sci*, 2022, 65: 139301
- 36 Peebles P Z. *Radar Principles*. Chichester: John Wiley and Sons, 1999
- 37 Balasubramanian R, Ponnusamy S, Vuorinen M. Functional inequalities for the quotients of hypergeometric functions. *J Math Anal Appl*, 1998, 218: 256–268
- 38 Shnidman D A. Determination of required SNR values. *IEEE Trans Aerosp Electron Syst*, 2002, 38: 1059–1064
- 39 Wang H K, Liao G S, Xu J W, et al. Subarray-based coherent pulsed-LFM frequency diverse array for range resolution enhancement. *IET Signal Process*, 2020, 14: 251–258
- 40 Wang H K, Liao G S, Xu J W, et al. Space-time matched filter design for interference suppression in coherent frequency diverse array. *IET Signal Process*, 2020, 14: 175–181
- 41 Mahafza B R. *Radar System Analysis and Design Using MATLAB (vol 3)*, Chapter 13. Beijing: Publishing House of Electronics Industry, 2016

## Appendix A Detailed procedures of shnidman function

In [38], a series of functions are proposed by David A. Shnidman to provide empirical approximation of the required single-pulse SNR for Swerling mode fluctuation target with certain requirements, including  $P_d$ ,  $P_{fa}$  and integration number  $n_p$ . Shnidman function is constructed by a series of equations as follows:

$$K = \begin{cases} \infty, & \text{Swerling 0,} \\ 1, & \text{Swerling 1,} \\ n_p, & \text{Swerling 2,} \\ 2, & \text{Swerling 3,} \\ 2n_p, & \text{Swerling 4,} \end{cases} \quad (\text{A1})$$

$$\alpha = \begin{cases} 0, & n_p < 40, \\ 0.25, & n_p \geq 40, \end{cases} \quad (\text{A2})$$

$$\eta = \sqrt{-0.8 \ln(4P_{fa}(1 - P_{fa}))} + \text{sgn}(P_d - 0.5) \sqrt{-0.8 \ln(4P_d(1 - P_d))}, \quad (\text{A3})$$

$$X_\infty = \eta \left( \eta + 2\sqrt{\frac{n_p}{2} + (\alpha - 0.25)} \right), \quad (\text{A4})$$

$$C_1 = \{[(17.7006P_d - 18.4496)P_d + 14.5339]P_d - 3.525\}/K, \quad (\text{A5})$$

$$C_2 = \frac{1}{K} \left\{ \exp(27.31P_d - 25.14) + (P_d - 0.8) \left[ 0.7 \ln \left( \frac{10^{-5}}{P_{fa}} \right) + \frac{(2N - 20)}{80} \right] \right\},$$

$$C_{\text{dB}} = \begin{cases} C_1, & 0.1 \leq P_d \leq 0.872, \\ C_1 + C_2, & 0.872 \leq P_d \leq 0.99. \end{cases} \quad (\text{A6})$$

Defining  $C = 10^{C_{\text{dB}}/10}$  and the calculated single-pulse required SNR  $\chi_1$  is given as

$$[\chi_1]_{\text{dB}} = 10 \log_{10} \left( \frac{C \cdot X_\infty}{n_p} \right). \quad (\text{A7})$$

Furthermore, Shnidman function has a wide range of application, which is suitable for  $0.1 \leq P_d \leq 0.99$ ,  $10^{-9} \leq P_{fa} \leq 10^{-3}$  and  $1 \leq n_p \leq 100$ , and its estimation error is less than 0.5 dB. Consequently, in Section 3, the Shnidman empirical function is utilized to estimate the required single-pulse SNR.